Optical Engineering

SPIEDigitalLibrary.org/oe

Comparison of coherent and incoherent laser beam combination for tactical engagements

Noah R. Van Zandt
Salvatore J. Cusumano
Richard J. Bartell
Santasri Basu
Jack E. McCrae
Steven T. Fiorino

SPIE

Comparison of coherent and incoherent laser beam combination for tactical engagements

Noah R. Van Zandt
Salvatore J. Cusumano
Richard J. Bartell
Santasri Basu
Jack E. McCrae
Steven T. Fiorino
Air Force Institute of Technology
Center for Directed Energy
Department of Engineering Physics
2950 Hobson Way
Wright-Patterson Air Force Base, Ohio 45433
E-mail: Salvatore.Cusumano@AFIT.Edu

Abstract. The performance of a multibeam laser system is evaluated for coherent and incoherent beam combination under tactical scenarios. For direct comparison, identical aperture geometries are used for both, coherent or incoherent, combination methods. The analysis assumes a multilaser source coupled with a conventional 0.32 m diameter, on-axis, beam director. Parametric analysis includes variations over residual errors, beam quality, atmospheric effects, and scenario geometry. Analytical solutions from previous results are used to evaluate performance for the vacuum case, providing an upper bound on performance and a backdrop for organizing the multitude of effects as they are analyzed. Wave optics simulations are used for total system performance. Each laser in the array has a wavelength of 1.07 μm, 10 kW (25 kW) output power, and Gaussian exitance profile. Both tracking and full-aperture adaptive optics are modeled. Three tactical engagement geometries, air to surface, surface to air, and surface to surface, are evaluated for slant ranges from 2.5 to 10 km. Two near-median atmospheric profiles were selected based upon worldwide climatological data. The performance metric used is beam propagation efficiency for circular target diameters of 5 and 10 cm. [DOI: 10.1117/1.OE.51.10.104301]

Subject terms: atmospheric propagation; coherent and incoherent laser beam combining; confidence intervals for wave optics; fiber lasers; laser arrays; waveguide lasers.

Paper 120899 received Jun. 21, 2012; revised manuscript received Aug. 31, 2012; accepted for publication Sep. 4, 2012; published online Oct. 10, 2012.

1 Introduction

Waveguide laser technology has rapidly advanced in the past decade and has garnered favor over chemical laser sources for future directed energy (DE) applications.[1] Waveguide lasers include both fiber lasers and planar waveguide lasers. The first, fiber lasers, has received abundant attention as a possible replacement for a chemical device. Fiber lasers have the beneficial features of long lifetimes, high efficiency,[2] and high beam quality.[3] A single mode fiber laser can now provide multiple kilowatts of power at wall plug efficiencies >25%.[4] The weight-to-power ratio for fiber lasers is approaching that of chemical devices.[5] But, at 10 kW per fiber, multiple sources must be combined to achieve useful power levels for tactical applications. Since fiber lasers at these power levels have too broad of an optical bandwidth for practical phasing, multiple sources would be used in a power adding architecture, also called incoherent beam combining (IBC). In contrast, narrow bandwidth, single-mode fiber lasers are currently limited to power levels below 1 kilowatt, else nonlinear effects dominate and destroy performance.[3,6,7] Coherent phasing of narrowband fiber lasers has been demonstrated for 32 fiber lasers with residual phase errors less than $\lambda/70$ root-mean-squared (RMS).[8] Even though no apparent limit exists for coherent beam combining (CBC) hundreds of narrow band fiber sources,[9] the risk due to practicalities of such a system must be considered high.

Another waveguide laser type, the *planar* waveguide laser, such as that being researched by Raytheon, shares many of the advantages of fiber lasers and is showing promise in meeting power levels >10 kW levels with narrow line widths of <10 MHz.[10,11] With these new developments in narrow band, kW-power sources, it is possible to consider the design tradeoffs between identical projecting apertures for both coherent and incoherent beam combining of multiple sources for use in a tactical DE system. Previous articles have considered such topics, but their designs used different aperture geometries for the coherent and the incoherent cases.[4,12] Comparing performance over different aperture geometries is both limited in scope and difficult to apply in general. This work starts by defining identical aperture geometries and power levels for both CBC and IBC, and provides detailed analysis to develop a fundamental understanding of the various tradeoffs between the two combination methods.

The remainder of the paper begins with a definition of a design that is amenable for either CBC or IBC. Theoretical analysis is presented that can model either CBC or IBC of the proposed aperture geometry with the proper choice of piston variation between the pupil subapertures. Numerical methods are used to analyze the effects of subaperture piston and tilt errors on performance, as well as the effects of beam profile, target size, fill factor, and aperture geometry. Since the

0091-3286/2012/$25.00

design uses a single tracker to point the aperture, the effects of pupil mismatch first presented by Fried and Greenwood, are evaluated.[13–15] Wave optics simulations allow for a complete evaluation of sensitivity and combined effects, including beam quality, platform jitter, adaptive optics, and thermal blooming. The wave optics simulations use a median-atmosphere for absorption and scattering levels with two turbulence levels. The impact of turbulence distribution on performance is included by defining and analyzing performance over three tactical engagement geometries. The paper concludes with a summary of performance of a system with nominal values for all parameters which are considered achievable with current technology. In general, it is shown that CBC always outperforms IBC for tactical engagements with a minor exception. This exception is discussed in detail throughout the paper. The paper provides sufficient comparison of the two methods to show the performance-benefit trade-off of coherent combination over incoherent combination.

2 Background

A typical, tactical architecture for the comparative evaluation of the key design issues for coherent beam combining (CBC) and incoherent beam combining (IBC) is shown in Fig. 1. Fan surveys current methods under study for beam combining.[6] Possible combination methods of multiple laser sources vary, but those methods applicable for tactical power levels can all be classified as either coherent or incoherent.[3,6] All proposed beam combination methods can be readily adapted to an architecture that uses a single beam director, i.e., a gimbaled telescope, for beam projection[5] as shown in Fig. 1. The architecture shown in Fig. 1 is considered the most practical and cost effective for the capabilities required to project a multilaser source in the case of either coherent or incoherent beam combining. This architecture allows for a direct comparison of coherent and incoherent combination without requiring new invention and its associated complexity. The beam director both transmits and receives allowing for proven solutions to pointing, tracking, and adaptive optics. Essentially, this architecture is an incremental change to any previously proposed DE tactical systems that would use a single source, but the design in this work presumes a multilaser source. Other approaches for IBC have proposed individual trackers, adaptive optics, and beam directors as a possible architecture.[4] The analysis within this paper is general enough to include this approach. The *on-axis* beam expander precludes a subaperture source on axis and, thus, reduces the fill factor (later defined in detail) leading to a reduction in propagation efficiency (also, defined shortly). However, the architecture is proposed as a design increment towards an optical phased array system which requires coherent transmitting and receiving,[12,16] through individual beam directors for each source element. In this respect, the paper concentrates only on the use of multilaser sources and directly compares the performance metric of propagation efficiency for the cases of incoherent and coherent beam combining. Less ambitious than an optical phased array system, this architecture has the advantage of lower cost with less technology development required for such a system and provides an intermediate look at the issues and advantages of phasing the source.

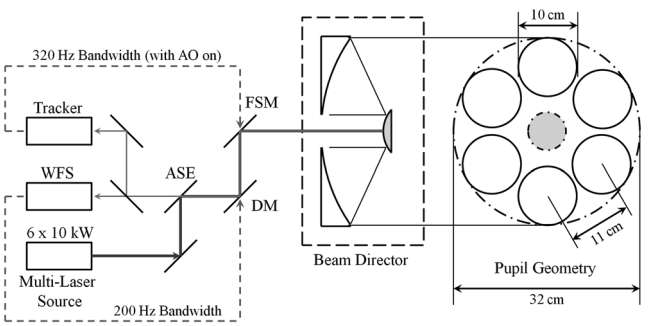

Fig. 1 Conceptual layout of a multilaser source with an on-axis beam director. This example considers a six-element source, each at 10 kW (60 kW) of power. As annotated, this architecture lends itself to a single tracker and possible adaptive optics system. Note that this layout, while allowing direct comparison of CBC and IBC, produces a relatively low fill factor. The aperture sharing element (ASE) combines the tracker and wavefront sensor (WFS) lines-of-sight before the deformable mirror (DM).

An IBC methodology that optically overlays multiple sources with spectral combining, polarized beam splitters, or dichroic beam splitters, provides a full beam at the pupil of the transmitter indistinguishable from that of single source with the same total power. The analysis of propagation performance of this IBC system is equivalent to that of a single beam source, and as such, is not addressed here. The remaining beam combining approaches can all be accommodated efficiently into the architecture of Fig. 1. More importantly, the analysis within provides a direct comparison of CBC and IBC with identical transmitting architectures, i.e., the geometry in the pupil is unchanged in comparison. This distinction separates this paper from previous references (see Refs. 4 and 17). The performance measure, propagation efficiency, is the ensemble averaged, integrated power over standard target sizes normalized by the power in the exit pupil of the transmitter. This metric is identical to previously published analysis and links the results directly for independent, follow-on lethality analysis.

The system design analyzed in this paper consists of a traditional 0.32 m diameter, on-axis beam director with a 20% central obscuration, where the monolithic laser is replaced by six tiled lasers, also referred to as subapertures (see Fig. 1). The subapertures are arranged in a hexagonal-pattern with expanded dimensions of 10 cm diameter, d, at the exit pupil of the beam director and 11 cm center-to-center separation, 's.' Each subaperture projects a 10 kW laser beam that is spatially coherent. The subaperture beams are collimated before the beam director and focused on target with the monolithic telescope optics of the beam director. The analysis assumes that coherent combining occurs in compact space (before beam expansion), but does not consider any specific method for phasing in detail nor phasing on target. Rather, the analysis parameterizes phasing performance by including residual beamlet tilt and piston errors for each subaperture.

Considerable research is currently addressing coherent combination to achieve tactical power levels as a viable alternative to a single, solid state source.[7,18–21] Coherent combination increases the peak irradiance proportional to N^2 by phase matching the output of each source, were as, incoherent combining gives an irradiance that is linear in the number of apertures. The additional complexity in phasing the

sources merits analysis that addresses the tradeoff between coherent and incoherent performance.

2.1 *Description of Scenarios*

The analysis uses three typical, tactical scenarios for evaluating CBC and IBC. The turbulence being stronger near the surface impacts performance depending on the scenario geometry. The scenarios use the generic names; air-to-surface (A2S), surface-to-air (S2A), and surface-to-surface (S2S). The description of each, listed in Table 1, provides enough information to perform the paper's detailed analysis and to relate each to an individual service's tactical engagement. A2S represents an airborne laser moving toward and firing upon a stationary ground target. S2A is the reciprocal of A2S, and represents a stationary ground laser firing at an aircraft. S2S represents a ship-to-ship horizontal path engagement. The complete design space, used in conjunction with the scenario definitions found in Table 1, is listed in Table 2. The analysis to follow will vary the parameters listed Table 2, individually and in combinations, to show the effects on performance. Here, we provide a complete listing for convenient reference.

Table 1 Tactical scenario details.

Engagement	Parameter	Value
Air to surface	Slant range	2.5, 5, 7.5, and 10 km
	Platform altitude	1524 m
	Platform speed	100 m/s
	Platform heading	000 deg
	Target altitude	3 m
	Target speed	0 m/s
	Target heading	180 deg
Surface to air	Slant range	2.5, 5, 7.5, and 10 km
	Platform altitude	3 m
	Platform speed	0 m/s
	Platform heading	000 deg
	Target altitude	1524 m
	Target speed	100 m/s
	Target heading	180 deg
Surface to surface	Slant range	2.5, 5, 7.5, and 10 km
	Platform altitude	15 m
	Platform speed	0 m/s
	Platform heading	000 deg
	Target altitude	15 m
	Target speed	10 m/s
	Target heading	270 deg

3 Beam Combination Theory

The theory presented in this paper is based on work published by Butts.[18] Butts' development concentrates on Strehl performance of a phased array of coherent sources for various levels of subaperture piston and tilt disturbances. This paper uses the metric of beam propagation efficiency (BPE) which is the ensemble averaged, integrated power in a circular bucket in the target plane normalized by the total power in the exit pupil. This metric emphasizes the important system performance of energy coupling to the target and avoids esoteric nuances, such as irradiance profiles on target, not considered necessary in a comparative study. BPE is closely related to power in the bucket (PIB), but generalizes the concept as a neutral metric when comparing coherent and incoherent combining. Other common metrics, such as M^2 and Strehl ratio do not accurately describe the performance of coherently combined lasers.[7,8] The analysis considers two bucket sizes, a 5 cm diameter and a 10 cm diameter circular bucket. These sizes represent typical target sizes for a tactical laser weapon.

3.1 *Subaperture Piston and Tilt Errors*

The focused irradiance pattern at the target plane is developed by modeling a coherent array with each subaperture field being uniform and containing terms to account for subaperture tilt and piston. The modulus squared of the combined fields can then model either a coherent array, by using little or no piston variations, or an incoherent array by choosing a high enough piston variation. The analysis assumes that the tilt and piston variations are equal in magnitude and pair-wise independent. This is reproduced from Butts.[18]

Define a uniform field across each individual subaperture as

$$U_n(\vec{r}_1) = (P/A)^{1/2} \exp\{i\vec{k}[a_n + b_n(x_1 - \bar{x}_n) + c_n(y_1 - \bar{y}_n)]\}, \quad (1)$$

where $U_n(\vec{r}_1)$ is the field over the nth subaperture centered at $(\bar{x}_n, \bar{y}_n)$, P is the power in the nth subaperture, A area of a single subaperture, $\vec{k}$ propagation vector with magnitude $2\pi/\lambda$; where a_n, b_n, and c_n are independent Gaussian random variables, a_n is the piston over the nth-subaperture; b_n and c_n are the x-and y-tilt, respectively, over the nth-subaperture, $\langle a_n^2 \rangle = \sigma_p^2$ and $\langle b_n^2 \rangle = \langle c_n^2 \rangle = \sigma_T^2$ with the angle brackets signifying ensemble averaging.

The total focused field of the array in the target plane (neglecting leading phase terms) is then[22]

$$U(\vec{r}, z) \simeq 1/(\lambda z) \sum_{n=1}^{N} \int_A U_n(\vec{r}_1) \exp(-i\vec{k} \bullet \vec{r}_1/z) d^2\vec{r}_1. \quad (2)$$

The ensemble averaged, focused, far field irradiance is calculated in Ref. 18 as

Table 2 System design space.

Category	Parameter	Values
Laser	Wavelength	1.07 μm
	Aperture configuration	6 Circular subapertures in a 32 cm on-axis beam director
	Total power	160 Hz Error rejection, 320 Hz Error rejection, both with 6 dB overshoot
Beam control	Track bandwidth (no AO), With AO	160 Hz Error rejection 320 Hz Error rejection 6 dB overshoot
	Adaptive optics, actuator spacing in exit pupil	0.02 m
	Adaptive optics, actuator grid	16×16
	Adaptive optics, bandwidth	200 Hz Error reject, 6 dB overshoot, Type 1[a]
Subaperture Phase error	Piston jitter, σ_p	0.0, 0.13, and 0.4, λ RMS
	Tilt jitter, σ_T	0, 0.1, 0.2, 0.4λ/d RMS
	Beam quality, BQ	1.0, 1.22, and 2.20
Full aperture	Tilt jitter, LOS_T	0.0, 5.0 μrads RMS
Atmosphere	Location	Kandahar, Afghanistan
	Season/time of day	Summer/0600, Summer/1500
Engagement	Air to surface ranges	2.5, 5, 7.5 and 10 km
	Surface to air ranges	2.5, 5, 7.5 and 10 km
	Surface to surface ranges	2.5, 5, 7.5 and 10 km

[a]Type 1: one free integrator in the forward control loop.

$$\langle I(\vec{r},z)\rangle = (P/\lambda^2 z^2 A)\left\{4Ad^2\int_0^1 \rho \mathrm{d}\rho\ \exp\{-k^2\sigma_T^2 d^2\rho^2/2\} \times\left[\cos^{-1}(\rho)-\rho\sqrt{1-\rho^2}\right]J_0(kdr\rho/z)\right\} + 4\pi^2\exp(-k^2\sigma_p^2)\sum_{n\neq m}^{N}\exp\{-ik\vec{r}\bullet(\vec{r}_n-\vec{r}_m)/z\} \times\left[\int_0^{d/2} r_1 \mathrm{d}r_1\ \exp\{-k^2\sigma_T^2\sigma_1^2/2\}J_0(krr_1/z)\right]^2, \tag{3}$$

where J_0 is a Bessel function of the first kind and all other terms have been defined previously, d is the diameter of a subaperutre, r_n is the vector location of the center of the nth—subaperture, r is the radial distance in the far field; and z is the distance to the far field pattern.

This analytical formulation provides an envelope of performance that provides intuition before proceeding to a wave optics simulation. A plot of BPE using Eq. (3) is instructive in understanding the tradeoffs between coherent and incoherent combining for the same pupil geometry. Figure 2(a) is a 3D plot of BPE for a 5 cm circular bucket with the beam focused at 7.5 km. The independent axes show the effect due to increases in subaperture RMS tilt jitter and subaperture RMS piston jitter as defined in Eq. (3), σ_T, σ_p, respectively. The plot on the top right [Fig. 2(b)] is for the case of subaperture tilt jitter only, while the plot on the bottom right [Fig. 2(c)] is for subaperture piston jitter only. Considering each effect individually, BPE approaches zero as subaperture tilt RMS is increased, yet the increase in piston RMS only shows that BPE asymptotes to the n-subaperture incoherent performance (IBC). The latter is intuitively pleasing since we would expect the subaperture beamlets to be completely incoherent with each other when the RMS disturbance approaches that for a uniform, random distribution over $\pm\pi$. The analytical model of the array for the range of 7.5 km and a 5 cm bucket shows CBC provides more energy on target than IBC. The assumption that this is strictly true for all ranges and bucket sizes though is not correct and leads to a key design tradeoff for a multiaperture system. This topic is addressed in detail in the subsequent sections.

3.2 *Comparison of Uniform and Truncated Gaussian Performance*

A plot of the ensemble averaged, integrated power as a function of bucket radius illustrates the tradeoff between CBC and IBC in more detail. The curves within Fig. 3 show this dependency for the same conditions of Fig. 2 where

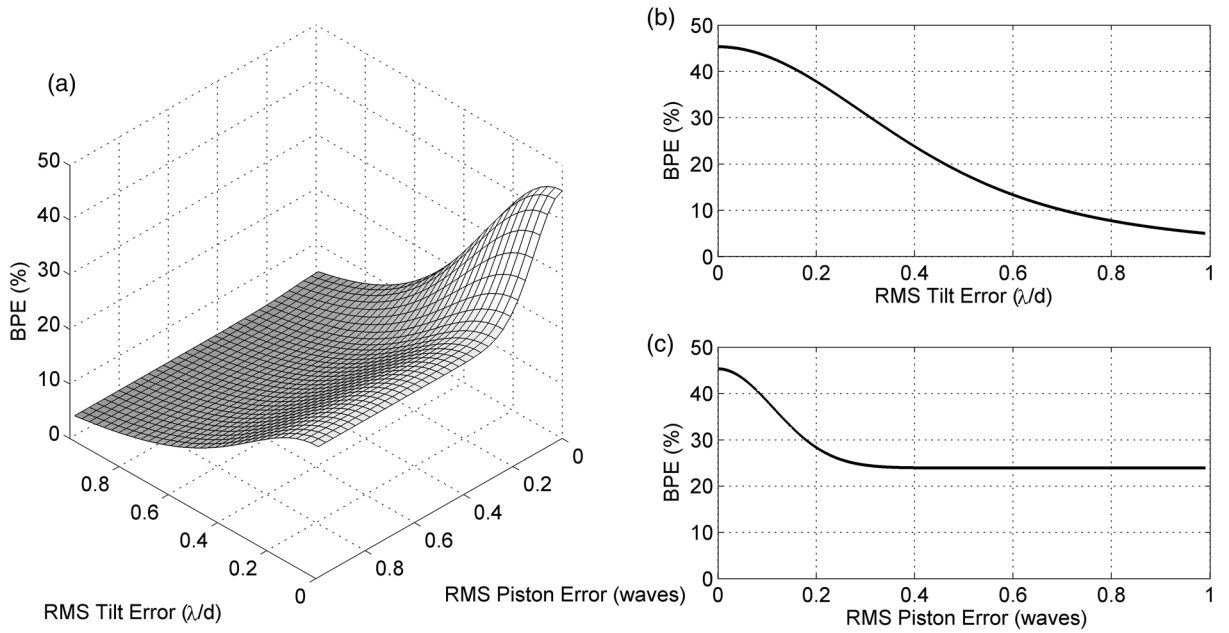

Fig. 2 Plot of BPE for the system defined in Fig. 1 focused at 7.5 km on a bucket with a 5 cm diameter. (a) The independent axes show the reduction in BPE for increasing subaperture tilt and piston RMS as defined in Eq. (1). (b) The subaperture tilt error reduces the PIB toward zero, while (c) the subaperture piston error only asymptotes to the completely incoherent beam combining level.

the array is focused onto a 5 cm diameter bucket at 7.5 km. Since Eq. (3) assumed a uniform field over each subaperture, the plot shows the integrated irradiance for both uniform and an optimally-truncated Gaussian waveform (i.e., 2.25 times the beam waist).[23] Both contain the same power out of the exit pupil. The solid lines are for the coherent case and the dotted curves are for incoherent combining. The first point is that the uniform wave provides more energy on target within the smaller buckets (note, describing this in terms of angular extent takes the range consideration out of the description)

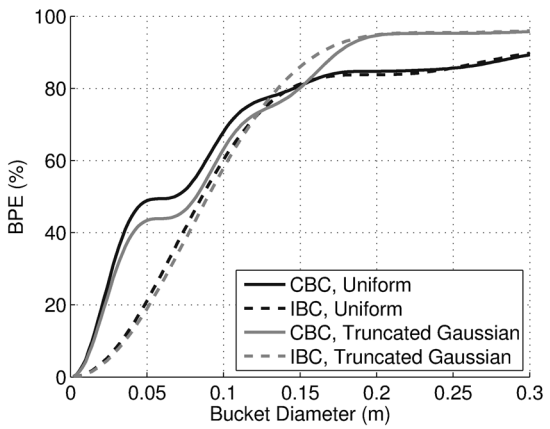

Fig. 3 Plot of integrated BPE of the system defined in Fig. 1 as a function of bucket radius for a beam focused at 7.5 km. This plot compares the integrated BPE for a uniform field and an optimally truncated Gaussian field over each subaperture. The solid curves are for CBC, the dashed are for IBC. Note that for the smaller bucket sizes, the uniform field over the subaperture diffracts more energy on axis. Not until a large radius bucket does the Gaussian field exceed the uniform in energy density. In the limit, the integrated energy curves come together as the bucket radius increases. These curves justify the use of a uniform field analysis as the envelope of far field performance for bucket radii that is a few multiples of the vacuum far field spot.

than the Gaussian waveform for CBC. It is only when bucket radii become relatively large that a Gaussian waveform surpasses integrated power of a uniform waveform for CBC. This point is moot, though, since IBC surpasses the integrated power of CBC for either Gaussian or uniform waveforms. Clearly, as the bucket size for BPE approaches the central lobe for a single subaperture, the integrated power of an array with Gaussian beams will exceed that of a uniform beam whether one considers the case for CBC or IBC. But, for these bucket sizes, the comparison between CBC and IBC breaks down since the aperture is not a free parameter in the analysis. The consideration of bucket sizes for BPE that approach the central lobe of a single subaperture implies that the wrong aperture geometry has been defined for the system. The conclusion: range and bucket size are key parameters that must be part of the definition of the aperture geometry. Once determined, CBC will provide the better BPE over IBC, regardless of beam shape. The analytical treatment using a uniform field is only a gauge for the best possible BPE since a uniform field (CBC or IBC) provides the higher power densities for the smaller bucket sizes. In the simulations that follow, a Gaussian beam is used due to the practicalities of waveguide lasers.

The consideration to optimize far field irradiance over a given angular extent in the far field opens up a new design dimension for DE systems not available in a monolithic beam design. The analysis within this work assumes that energy coupling into the target is limited to the first few radii of the coherent central lobe of the full aperture.

3.3 *CBC and IBC versus Bucket Size and Range*

The relationship between PIB and BPE is just the normalizing factor of total power out of the aperture, which for this case is 60 kW. What follows is given in terms of PIB to show the marginal differences between CBC and IBC as the angular extent of the bucket is made large. The comparison of PIB

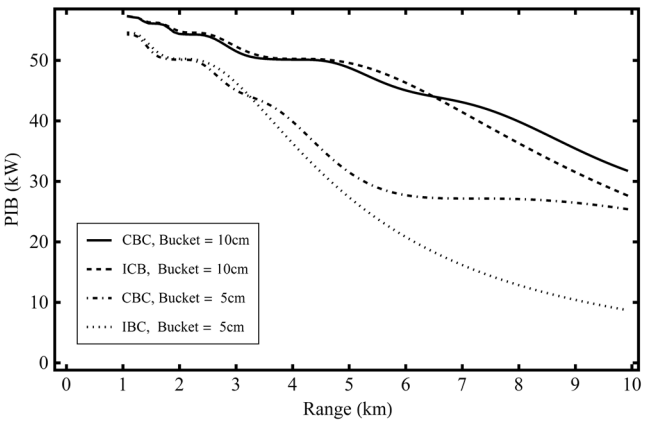

Fig. 4 Plot of PIB(z) of CBC and IBC. The comparison shows that as the bucket encircles multiple radii of the CBC far field central spot, IBC can have higher PIB. The plateauing of the CBC case for the 5 cm bucket at 6 km arises from the fill factor of the array.

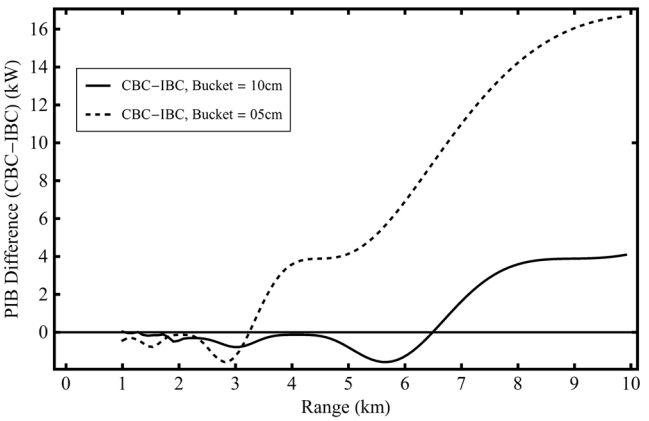

Fig. 5 Difference of CBC minus IBC PIB(z) presented in Fig. 4. These differences (CBC–IBC) are for the two bucket sizes, 5 cm and 10 cm. When the curves become positive, CBC encircles more power than IBC. This occurs when the angular extent of the bucket is only a few radii of the central spot of the full coherent aperture. As the angular bucket size becomes exceedingly large, then the PIB of IBC exceeds that of the CBC.

for a fixed radius bucket as the range increases is presented in Fig. 4. This figure contains PIB(z) for two bucket sizes and for both cases CBC and IBC. The bucket sizes are 5 and 10 cm and the PIB is for the vacuum case. Since the bucket size is fixed, as the range increases the angular radius decreases and eventually only encloses the central lobe of the coherent full aperture. This is manifest in the CBC curve for the 5 cm bucket size at 6 km where the curve levels off. The PIB level at this inflection is dependent on the 'fill factor,' F_f, of the array. For the uniform subaperture field, the fill factor is defined as the ratio of the total subaperture area divided by the total area that encloses the subapertures.[2] The fill factor for the system in Fig. 1 is calculated in Eq. (4) as,

$$F_f = \frac{n\pi(d/2)^2}{\pi(D/2)^2} = 0.586. \tag{4}$$

The value of PIB for CBC and for the given fill factor is then

$$\mathrm{PIB_{CBC}} = 0.586 * 0.84 * 60\mathrm{e}^3\mathrm{W} = 29.5\ \mathrm{kW}.$$

This agrees with the analytical model calculation in Fig. 4. The 0.84 factor is the percent of power of a monolithic circular aperture within the central lobe of the far field spot.

PIB differences, CBC-IBC, for the two bucket sizes, shown in Fig. 5, more readily displays the performance difference between the two methods of beam combining. CBC is providing more power in the defined bucket than IBC when the curves are positive. For ranges where the angular radius of the bucket is relatively small, the CBC captures more PIB than IBC. In general, these are typical bucket sizes well below the central lobe of a single subaperture. As discussed in Sec. 3.2, for large angular bucket sizes, these curves clearly show that IBC captures more power than CBC. But, again, to conclude that IBC is better than CBC for the close in ranges is to miss the point that a CBC design for this range and bucket size can be defined to outperform IBC. Also, the differences are marginal for the shorter ranges and CBC clearly provides performance out to significantly further distances.

3.4 *Exit Pupil Scaling*

The previous discussion established design considerations for identical geometries given target ranges and vulnerable area diameters. The following establishes a framework to understand the design trade-offs for changes to the exit pupil geometries. The PIB for various configurations of the exit pupil are shown in Fig. 6. All configurations transmit the same amount of power. The solid curve is the encircled power for the IBC case for six subapertures. The dotted curve just above the solid line is the encircled power for the CBC. These represent the baseline design of Fig. 1 and are the same curves for uniform subaperture illumination as shown in Fig. 3. If the fill factor is changed by reducing the subaperture diameter and then using two rings to fill the 30 cm exit pupil, the first plateau rises indicating the higher power densities due to the increased fill factor. If instead, the same fill factor is maintained, but the diameter of the exit pupil is

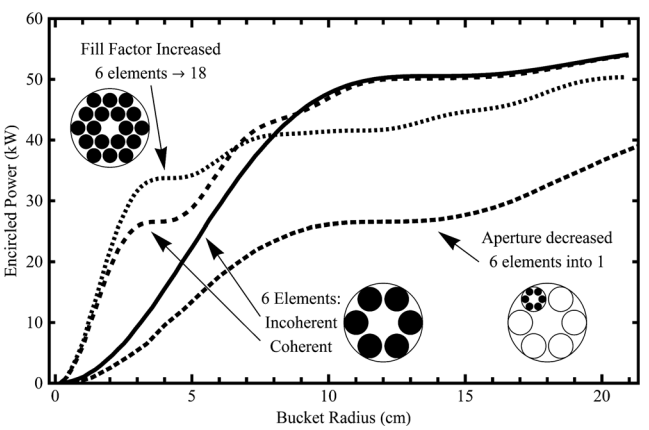

Fig. 6 Encircled energy for various exit pupil geometries in vacuum. All configurations transmit the same amount of power. The solid line curve is the PIB for the IBC case. The 6 element CBC case as introduced in Fig. 1 is the dotted curve just above the IBC case. If the number of subapertures is increased over the same exit pupil diameter, the power density is increased as shown by the short-dotted line. Keeping the fill factor the same, but decreasing the exit pupil diameter by a factor of 3, changes the PIB curve to the dashed line.

scaled down by a factor of 3, the encircled power is now spread out to the wings lowering the power density in the center (shown as the dashed line). (Not shown is the IBC case for the 18 subapertures. This curve would have fallen well below the 6-subaperture IBC case.)

This single plot displays the key tradeoffs for exit pupil geometries when comparing CBC and IBC. The comparison clearly shows that fill factor raises the power density near the center of the optical axis while keeping the same fill factor but reducing the size of the exit pupil diameter scales the power density by the same ratio as the change of diameters, but to larger angles in the far field. Note that the two 6 element arrays plateau at the same level, but the smaller aperture does so at a larger radius.

3.5 *Aperture Mismatch*

The architecture presented in Fig. 1 uses a full aperture tracker to provide tilt corrections for the subaperture pointers. This is proposed for design economy and simplicity. However, since the subapertures are smaller than the whole aperture used by the tracker and since they are displaced from the centerline of the tracker line-of-sight (LOS), their pointing will be incorrect to some degree. The magnitude of this error is dependent upon the tracker error rejection bandwidth, turbulence strength, and the effective crosswind. Reference 13 provides a complete development of this error with further study in Refs. 14 and 15. The analysis in this work considers the three scenarios defined in Sec. 2.1. Recall, they are described as air-to-surface (A2S), surface-to-air (S2A), and surface-to-surface (S2S). The curves presented in Fig. 7 are for the case of no AO and plot RMS tilt error for an individual subaperture as a function of tracker error rejection bandwidth. The errors decrease initially as the tracker error rejection bandwidth increases. For the geometry described in the paper, the errors reach near minimum value at a bandwidth of around 50 Hz. Any further increase in the error rejection bandwidth does not reduce the tilt error appreciably since the correlation of tilt between the mismatched pupils is lower for the higher frequencies. Note with no AO, the magnitude of the minimum error can be quite high for the S2A and S2S scenarios. For these scenarios the error ranges from $0.4\lambda/d$ to λ/d, where d is the diameter of a subaperture. In contrast, the A2S scenario, however, shows a much smaller error of $0.13\lambda/d$ with no AO. The difference in pupil mismatch tilt error between the A2S and the S2A is due to the turbulence strength near the aperture being lower for the A2S scenario. As the beam propagates to the target, any phase effects that would cause a tilt have less path length to manifest as an error. When an AO subsystem corrects for turbulence across the full aperture the tilt error due to pupil mismatch is mitigated significantly. With AO, the minimum error in all 3 scenarios is reduced to approximately $0.1\lambda/d$. Thus, as a cautionary note, it would not be prudent to implement a candidate design as presented in Fig. 1 for S2A or S2S, for either CBC or IBC, without due consideration of the impact of this error in pointing.

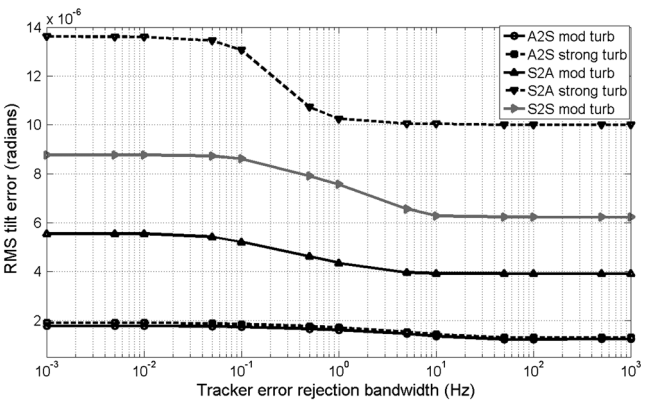

Fig. 7 Subaperture pointing tilt error due to full aperture tracker without AO. The tilt error is a function of both the turbulence and the tracker's error rejection bandwidth. This tilt error is mitigated significantly when an AO subsystem corrects for turbulence across the full aperture. For all systems analyzed in this work, the error with AO is reduced to less than $1/10\ \lambda/d$, where, d is the diameter of the subaperture.

4 Wave Optics Simulations

In the previous section, we used theory to compare and analyze CBC and IBC. Now, we include control loops and all atmospheric effects by using wave optics simulation. The wave optics simulation models the atmospheric turbulence and thermal blooming effects; full aperture tracker and adaptive optics; subaperture residual phase and tilt; and subaperture wavefront beam quality. The wave optics simulations were performed with a detailed model assembled in WaveTrain®. Wave optics simulations normally model coherent waveforms, therefore, a method to model the incoherent array was devised for this work. WaveTrain modeled the coherent and incoherent array with the same simulation structure and modeled each case by adding various amounts of random piston to each subaperture field on a frame-by-frame basis. In this way, low-level disturbances were added to model residual errors of a finite-bandwidth phasing loop for the coherent case while higher levels of piston variation were added to model an incoherent array. For the coherent case, the fields are added in the target plane before calculating the total irradiance. For the incoherent case, the piston variances are large to model temporal incoherence and the subaperture *irradiances* are added in the target plane to model the lack of coherence between the subapertures.

4.1 *Wave Optics Setup*

The subaperture waveforms in the simulation are modeled as truncated Gaussian beams since this is expected to well model the likely beam shape from a waveguide source. Each Gaussian beam (also referred to as a 'beamlet') is truncated at $d = 2.25w_0$, where w_0 is the $1/e^2$ irradiance radius of the Gaussian beamlet and d is the diameter of the truncating aperture. The transmitted power at the exit pupil is set after truncation to be the same in all cases. Such truncation produces maximum on-axis intensity for a single laser source.[22] For the case of coherent combination, the optimal sizing would be about $d = 2.13w_0$.[19] To allow direct comparison of performance, the analysis uses the same size, $2.25w_0$, for all analysis of CBC and IBC. It should be noted that performance on-axis for CBC could be slightly increased by optimally sizing the beamlets for the CBC case. Performance could also be slightly increased for the cases with tilt jitter, σ_T, if the beamlets were resized according to Yura's equations (see Ref. 24). Additionally, the truncation to

maximize PIB for a certain target size could differ from that to maximize on-axis intensity. The analysis for optimizing PIB as a function of subaperture field is left as a follow on report. In this work, however, the authors do not expect these possible changes in truncation and subaperture fields would alter the conclusions of this paper in any way.

The wave optics simulation includes all effects from exit aperture to the target. A point source is used as a target to simplify the analysis of coherent versus incoherent beam combining. The simulation adds random disturbances to model residual errors that would arise from the system's local tilt loop for the full aperture, and the tilt and phasing loops of the multilaser source. These disturbances are all considered pairwise independent. Each is modeled as a random variable with an underlying white, Gaussian distribution, with the RMS chosen to vary the magnitude of the disturbance. In addition to these residuals, the beam quality of each subaperture field can be degraded to model less than perfect sources. These disturbances and the effects they model are summarized as follows:

(1) LOS Jitter (LOS_T): Full aperture LOS jitter that models unsensed, on-board optical LOS variations due to base disturbances. The magnitude is set by the RMS value, LOS_T, of a white, Gaussian distribution.

(2) Subaperture random piston (σ_p): Array coherence is varied by adding a time varying piston to each subaperture. The magnitude is set by the RMS value, σ_p, of a white, Gaussian distribution. The RMS is varied in magnitude to simulate a coherent array with a low residual phase loop error or with large values to simulate an incoherent array.

(3) Subaperture random tilt (σ_T): This effect models residual tilt jitter from the on-board beam relay loop (not shown in Fig. 1). The magnitude is set by the RMS value, σ_T, of a white, Gaussian distribution.

(4) Subaperture beam quality (BQ): WaveTrain® models higher-order phase aberrations over each subaperture to account for reduced beam quality in each of the array sources. The beam quality phase is generated by summing Zernike polynomials of order 4 to 15 (Noll's ordering) with each radial order receiving an equal weighting of net wavefront variance totaling to σ^2_{WFE}. Beam quality uses the Maréchal approximation and the performance model[7] relating BQ to Strehl to arrive at the relationship $\mathrm{BQ} = \exp\left(\sqrt{2\pi}\sigma_{\mathrm{WFE}}\right)^2$.

The system degradations described above are used to model realistic systems and to evaluate the sensitivity of the system to these residuals. The wave optics simulation with the defined residuals then provides an evaluation of BPE. This metric is evaluated for three different scenarios, each for two different atmospheric conditions. The performance of a fully-coherent, *idealized* laser array would be simulated with the residual disturbance parameter set with $\mathrm{LOS}_T = 0$, $\sigma_p = 0$, $\sigma_T = 0$, and $\mathrm{BQ} = 1$.

Figure 8 is an instance of the subapertures' fields, each with either random piston [Fig. 8(a)], random tilt [Fig. 8(b)], or random higher-order phase error to model a reduction in beam quality [Fig. 8(c)].

The wave optics model also includes control loops for full-aperture tracking and adaptive optics. The full transmitting aperture is used to collect target radiance and is spectrally shared with a single, full aperture tracker and adaptive optics (AO) system. The tracker controls a single fast steering mirror (FSM), which corrects all beamlets using the measured, full aperture tilt of the line-of-sight (LOS) to the target. The tracker has two bandwidths: 160 Hz error rejection for track only mode and 320 Hz when the AO subsystem is closed loop. Both loops have a nominal 6 db of overshoot. The higher tracker bandwidth was used to accommodate the higher frame rates used for the AO subsystem.

The AO subsystem uses full aperture measurements with a Shack-Hartmann wavefront sensor (WFS) and a single deformable mirror (DM) to correct for higher order atmospheric disturbances. The DM has a 16×16 square grid of actuators truncated by the 32 cm diameter aperture. The AO error rejection bandwidth is 200 Hz with 6 db of over shoot. The analysis to follow will report results with and without the AO in operation. A list of pertinent parameters for the laser aperture and beam control subsystem are given in Table 2. Figure 9 shows, qualitatively, the effect that AO can have on both CBC and IBC far-field spots for the surface to air case at 7.5 km range with no subaperture phase errors or platform jitter. The left column is CBC, while the right is IBC. The first row shows the far-field spots with no turbulence, while the second row includes turbulence, visibly degrading both CBC and IBC spots. The last row includes both turbulence and AO, showing that AO does reduce turbulence degradations.

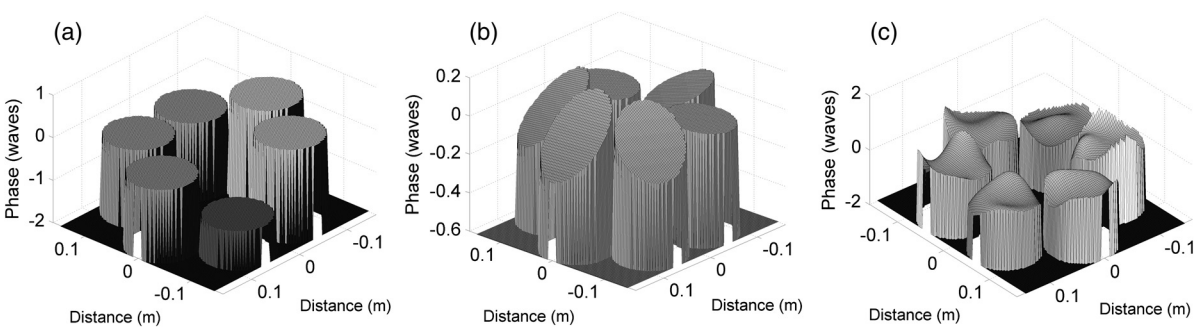

Fig. 8 The OPD of the beamlets for incoherence, tilt jitter error, and imperfect beam quality: (a) shows the OPD for incoherent combination ($\sigma_p = 0.4\lambda$) for a single time instance, (b) shows the OPD with $0.4\lambda/d$ differential jitter (σ_T), and (c) shows the OPD for poor beam quality (BQ = 2.20).

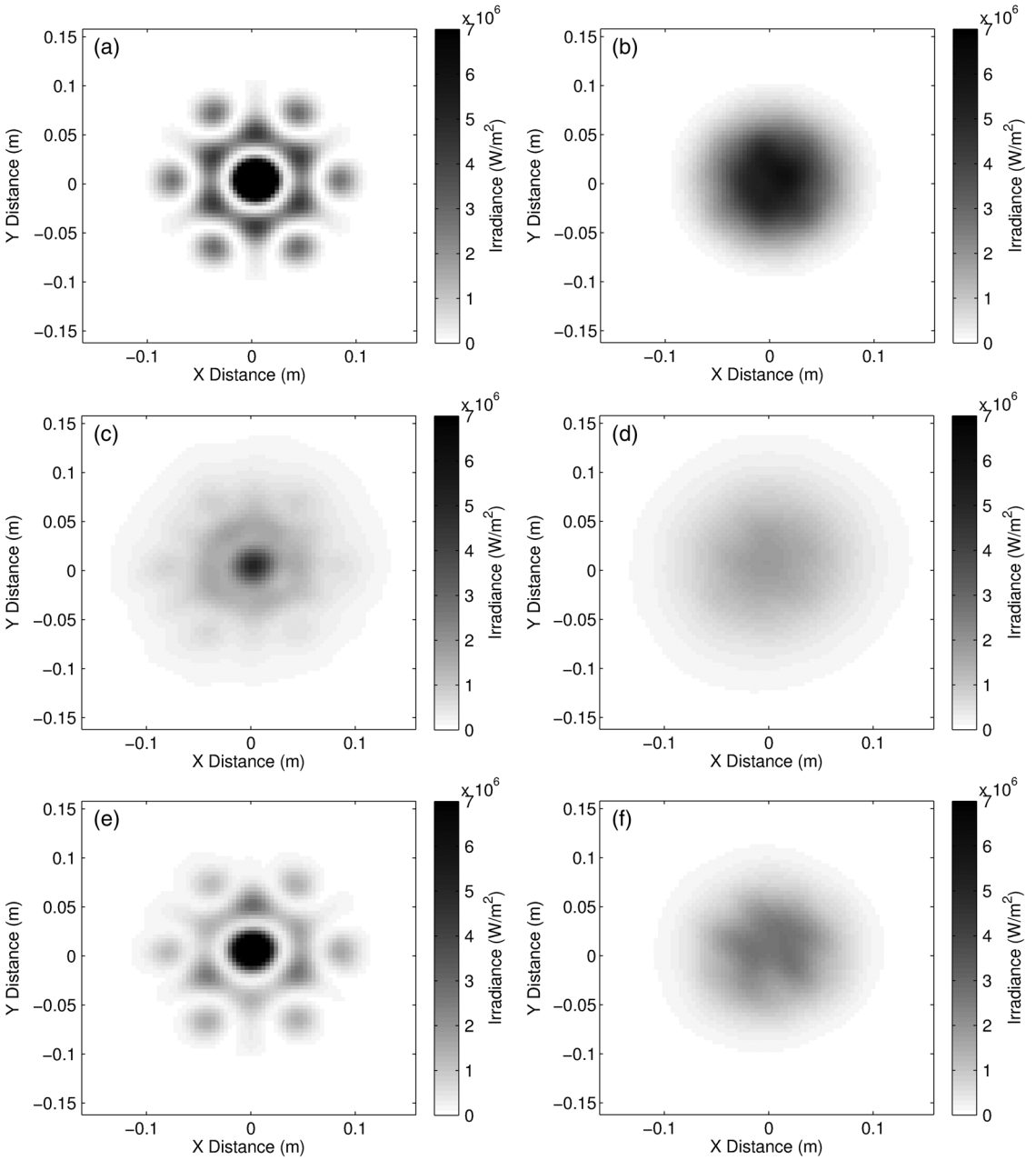

Fig. 9 The far-field spots for the surface to air engagement after propagating 7.5 km. (a) The spot for coherent beam combination with no turbulence is tightly-focused with a bright central lobe and distinct side lobes. (b) For incoherent combination with no turbulence, the spot is Gaussian and much less intense than the coherent spot. (c) and (d) When moderate atmospheric turbulence is included, the far-field CBC and IBC spots are noticeably distorted. (e) and (f) Adaptive optics can correct some of the turbulence, increasing intensity for both CBC and IBC. The scale is the same for all plots. Simulation conditions: surface to air engagement, 7.5 km range, 5 cm bucket, moderate turbulence (when included), 60 kW array, $\mathrm{LOS}_T = 0$, $\sigma_T = 0$, $\sigma_p = 0$, BQ = 1.0.

4.2 *Description of Atmospheric Conditions*

The atmospheres chosen for this work are based on parameter and particle distributions constructed by the laser environmental effects definitions and reference (LEEDR) software package using the ExPERT database. The ExPERT database contains world-wide, climatological data recorded over approximately the last thirty years for 573 worldwide sites. LEEDR uses the observations recorded at these sites to estimate the average transmission within the boundary layer for each location. After forming a cumulative distribution of transmissions at the 1.07 μm wavelength, we selected a value close to the worldwide median for tactical engagements. The surface conditions associated with this site provided a consistent parameter set to model the most probable atmospheric condition. The site associated with the median transmission was Kandahar, Afghanistan.

LEEDR provided high-fidelity profiles of absorption, scattering, and turbulence for the selected atmospheres at 1.07 μm. Figure 10 shows the two components of atmospheric extinction, absorption and scattering, for the two selected profiles above Kandahar, one for 0600 and the other for 1500 local time. As the surface temperature rises

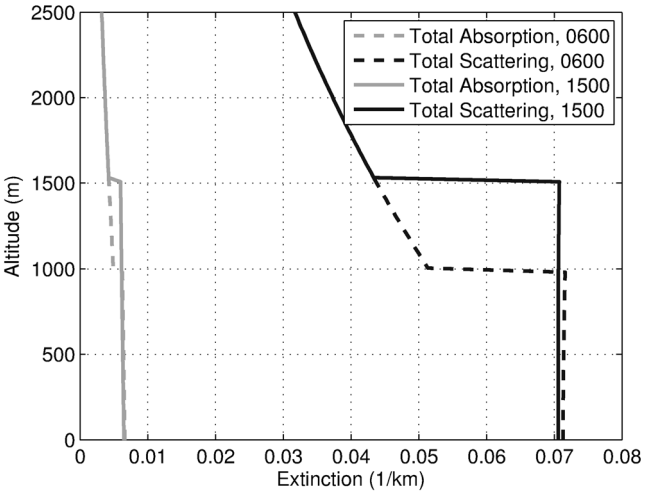

Fig. 10 The total (molecular and aerosol) absorption and scattering profiles from LEEDR at 1.07 μm for Kandahar, Afghanistan in the summer at 0600 and 1500 local time. Note that the boundary height rises in the afternoon.

in the afternoon, the boundary layer height and thickness increases accompanied by a corresponding increase in turbulence. LEEDR modifies the lower portion of the Hufnagel-Valley (HV) profile to account for the change in turbulence strength as the surface temperature increases. This modification is based on the McClung-Tunick model developed by the Air Force Institute of Technology,[25,26] which more accurately accounts for turbulence in the first 50 m above the surface. Above 50 m, the turbulence profile blends with the Hufnegel-Valley 5/7 profile. Figure 11 shows the turbulence profiles used for the two different times. Note that below 50 m altitude at 0600, the predicted turbulence levels are lower than the HV 5/7 profile. The results presented in Sec. 5 use the atmospheric conditions for Kandahar for 0600 and 1500 local to represent a moderate and a high turbulence case, respectively.

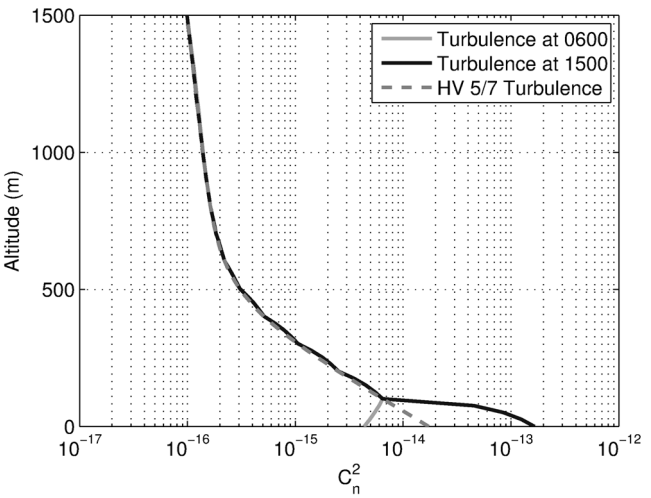

Fig. 11 The Hufnagel-Valley and modified Hufnagel-Valley turbulence profiles used in our evaluation. The difference in the first 50 m above the surface accounts for surface heating during the day. The modification is based on research into atmospheric modeling at the Air Force Institute of Technology.

4.3 *Numerical Considerations*

The wave optics simulation is the most appropriate method for analysis beyond what can be done with theory, but requires due consideration in generating reliable results. Recognizing that Cn^2 is only a parameterization of the variability of a given atmosphere, a performance data point for PIB consists of an average over thirty experiments of the same scenario with each experiment using a different random realization of the atmosphere for the given Cn^2. The PIB calculated from a single experiment is the average PIB over the last 50 ms of the time simulation. Choosing the last 50 ms of PIB in the experiment avoids transients due to the tracker and AO responses and ensures the thermal model of the beam-atmosphere interaction has reached steady-state. Figure 12 displays the variability in PIB (dots) over different atmospheric realizations (i.e., for 30 different experiments) for the surface to air engagement. The solid line is the running average of the PIB over the experiment number. The dotted curves enclosing the running mean of PIB show the 95% confidence interval. Table 3 shows the percentages for 95% confidence intervals for the three scenarios. The limits shown bracket the confidence intervals calculated for the three scenarios for the moderate and high turbulence atmospheres. The conditions for the two intervals are listed in the table. The greatest variability occurs for the S2S scenario with a confidence interval just under 10%. Most others remain around 5%. The results reported for all cases in the remaining sections can be considered to have a 95% confidence interval for BPE when $+/-10\%$ of the values reported is applied.

5 Simulation Results and Comparison with Theory

In this section, we use the wave optics simulations just described to analyze performance of the conceptual system

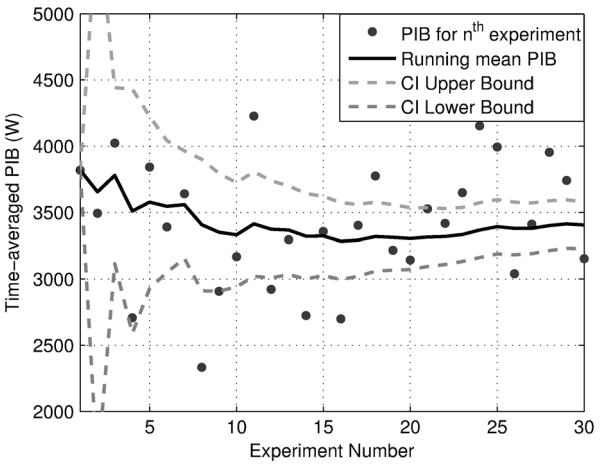

Fig. 12 The dots show the time-averaged PIB over 50 ms of the steady-state condition of a single experiment. An experiment is defined as a simulation involving a single, random realization of atmospheric turbulence for a specific Cn^2 profile. A single PIB data point is obtained by averaging the PIB from all 30 experiments. All experiments use the same specification of atmosphere (moderate or high turbulence), engagement, AO or not, LOS_T, σ_p, σ_T, and BQ. The solid line is the running mean of PIB over the 30 experiments. The 95% confidence interval for 5 cm diameter PIB converges to $+/-5.18\%$ (dashed lines). Simulation conditions: S2A scenario, 7.5 km range, 5 cm bucket, moderate turbulence, 60 kW array, $LOS_T = 0$, $\sigma_T = 0$, $\sigma_p = 0.4\lambda$, BQ = 1.0, and no AO.

Table 3 Ninety-five percent confidence interval bounds (%) for the 7.5 km slant range.

Engagement	Air to surface				Surface to air				Surface to surface			
Turbulence	Moderate		High		Moderate		High		Moderate		High	
Bucket diameter	5 cm	10 cm	5 cm	10 cm	5 cm	10 cm	5 cm	10 cm	5 cm	10 cm	5 cm	10 cm
Benign case[a]	2.75	0.98	2.92	1.36	2.36	0.80	2.82	1.62	5.54	4.34	6.83	4.47
Stressing case[b]	5.80	2.78	5.89	3.23	5.51	2.15	7.15	5.13	8.91	7.07	7.29	4.77

[a]The benign case has zero piston error, zero subaperture tilt, a BQ of 1.0, no platform LOS jitter, and AO on. This combination generally produces the smallest confidence interval bounds.
[b]The stressing case is for incoherent combining and has 0.4 waves RMS piston error, 0.4 lambda/d differential tilt, a BQ of 2.2, 5 urad rms full aperture LOS jitter, and AO off. This combination generally produces the largest confidence interval bounds.

architecture of Fig. 1 for both CBC and IBC. The assumption adhered to is that the aperture diameter is given and fixed. This is not unreasonable, since the size of the beam director will be a major driver in system performance, its size would be made as large as feasible to extend range and reduce the effects of diffraction.[5] The theory-based curves shown in Figs. 4 and 5 clearly show that for the vacuum case and for the given fixed aperture geometry, CBC will always perform better than IBC for bucket sizes less than a few times the radius of the vacuum far field central lobe of the synthesized aperture.

Table 4 contains a partial summary of results comparing CBC and IBC starting with the vacuum case and successively including additional atmospheric effects. Tables 5 and 6 show the associated atmospheric and performance parameters commonly used to predict tracking and AO performance. The atmospheric and system parameters for each simulation are listed within Table 4. The sequential decrease in performance with the inclusion of more effects provides a look at the sensitivity of the system and an upper bound for corrective measures. This summary shows that under both moderate and high turbulence, CBC outperforms IBC. In some cases the performance increase may not justify the additional complexity of the phasing subsystem or the AO subsystem. It can also be noted from Table 4 that the CBC S2A case shows a significant loss due to atmospheric turbulence. This tags this scenario for consideration of an AO subsystem. Recall that with the absence of AO there is a reduction in BPE performance due the mismatch of pupils. The addition of AO will not only improve performance by correcting the higher order, but also in this case, by improving the subaperture pointing. Further, Table 4 shows that the S2S scenario is dominated by turbulence, as the addition of turbulence has by far the most degrading impact on BPE. Note the only slight reduction in the A2S scenario in turbulence implies AO may not be considered for a system that only flew A2S scenarios. Table 4 shows that for the 60 kW power level, thermal blooming has little impact on performance for all scenarios. An increase in power level is explored further in a later section. Lastly, note that the omission of BPE for the high turbulence S2S scenario. This is a stressing case for both CBC and IBC, but IBC, in general, will be more limited in range even with AO. This scenario is referred to as 'deep turbulence' and is the subject of ongoing research for CBC. Figure 13 presents BPE for both CBC and IBC for all three scenarios as a function of range. These plots clearly show the benefit of CBC over IBC. The log scale for performance reduces the graphical differences between CBC and IBC, also, we remark that BPE performance below 10% is not considered a viable mission.

5.1 *Impact of Subaperture Piston and Tilt Error, σ_p and σ_T*

The performance of CBC has been so far reported without residual errors that would be present in the phasing and pointing loops due to finite bandwidths. The next few

Table 4 BPE (%) for 60 kW, 7.5 km slant range, moderate and high turbulence, $LOS_T = 0$, $\sigma_p = 0$, $\sigma_T = 0$, and BQ = 1, full aperture tracker, no AO.

Engagement	Air to surface				Surface to air				Surface to surface			
Coherence	Incoherent		Coherent		Incoherent		Coherent		Incoherent		Coherent	
Bucket diameter	5 cm	10 cm	5 cm	10 cm	5 cm	10 cm	5 cm	10 cm	5 cm	10 cm	5 cm	10 cm
Diffraction-limited	17.5	55.1	44.4	64.0	17.5	55.1	44.4	64.0	17.5	55.2	44.4	64.0
Diff. and extinction	10.9	34.3	27.6	39.8	10.9	34.3	27.6	39.8	10.3	32.3	26.0	37.5
Diff., ext., and moderate turbulence	10.3	32.5	24.4	37.9	6.3	21.2	9.3	24.2	3.6	12.5	4.2	13.8
All above effects with thermal blooming	8.9	29.0	22.2	34.6	5.6	19.5	9.2	23.4	3.2	11.4	3.7	11.6
All effects, high turbulence	8.3	27.5	19.9	32.4	1.5	5.5	1.7	6.3	—	—	—	—

Table 5 Turbulence parameters for 7.5 km slant range.

Time of day	Engagement	Rytov value	Fried r_0 (m)	Greenwood (Hz)
0600	Air to surface	0.0733	0.300	34.3
	Surface to air	0.0733	0.0692	36.7
	Surface to surface	0.596	0.0428	62.2
1500	Air to surface	0.225	0.252	57.5
	Surface to air	0.2252	0.0264	61.6
	Surface to surface	18.17	0.0055	482

sections present a sensitivity study to the magnitude of these residuals, starting with the subaperture phase and tilt errors. The theoretical curves are plotted with use of Eq. (3) adjusted for atmospheric extinction over the 7.5 km path.

Figure 14 separately shows the sensitivity to subaperture tilt jitter, σ_T, and piston jitter, σ_p. As a point of reference, consider the A2S scenario. BPE is reduced by ~10% when all subapertures have a residual tilt jitter of $0.2\lambda/d$ RMS. This is considered significant and would require care in design, but not necessarily a stressing design requirement. Note the increased sensitivity to piston jitter versus subpaperture tilt jitter, but even with large increases in piston jitter, the BPE asymptotes to a level defined by the IBC of the array. This level can be seen in the figure to be a BPE of about 15% occurring at an RMS value of 0.28λ. For the A2S CBC scenario, keeping the reduction in BPE less than ~10% due to piston jitter alone requires an RMS value below 0.1λ. Given published results for phasing multiple sources report 0.03λ RMS or better in a laboratory environment this requirement is not considered stressing.[8]

Since the BPE plot versus piston RMS jitter in Fig. 14(b) spans values equivalent to an incoherent array, a comparison of IBC to CBC can be made by comparing the values to the right of 0.28λ RMS to those left of this point for CBC.

5.2 *Impact of Beam Quality, BQ*

The analysis included beam quality residual errors to specifically determine if its effects would be masked by moderate or high turbulence. The analysis that follows shows that beam quality directly impacts BPE even in strong turbulence and a reduction in beam quality is not masked with other beam spreading effects in a root-summed-squared (RSS) relationship. Figure 15 shows the dramatic drop in performance for both CBC [Fig. 15(a)] and IBC [Fig. 15(b)] for all three engagements as beam quality degrades for the case of a 7.5 km slant range, a 5 cm diameter bucket, and moderate turbulence.

Figure 15(a) shows BPE drops by 70% for the CBC air to surface case (30.0 cm r_0) as beam quality is reduced from 1.0 to 2.2. For the surface to surface engagement (4.28 cm r_0), the same change in beam quality reduces BPE by 54%. Figure 15(b) shows similar trends for IBC. Again, poor beam quality for IBC results in reduced performance for all engagements. Since BPE for IBC is lower than CBC for the better beam quality values, the reduction is less dramatic but still measureable.

Table 6 Fried coherence length across slant range.

Time of day	Range (m)	r_0 (m) Air to surface	r_0 (m) Surface to air	r_0 (m) Surface to surface
0600	2500	0.554	0.133	0.0827
0600	5000	0.366	0.0876	0.0546
0600	7500	0.300	0.0692	0.0428
0600	10000	0.241	0.0578	0.0361

5.3 *Impact of Platform Jitter, LOS$_T$*

Residual error in platform jitter is one of the major contributors to loss of energy on target in all laser systems.[5] The effects of subaperture jitter, σ_T, have already been presented, this section presents the impact when all beamlets are moving in unison, i.e., as coherent tilt jitter, previously

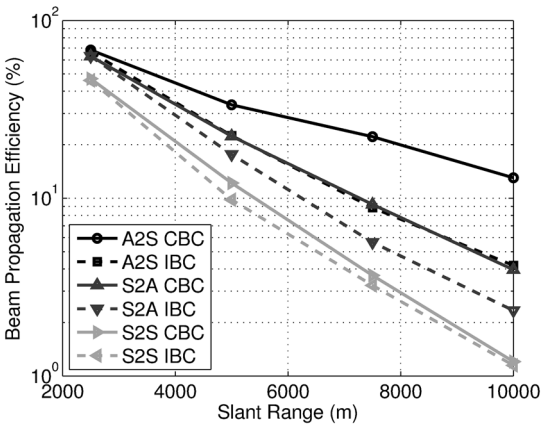

Fig. 13 Comparison of CBC and IBC beam propagation efficiency (BPE) from 2.5 to 10 km ranges for all three scenarios in moderate turbulence with a 5 cm bucket. CBC out performs IBC. The turbulence of the S2S scenario washes out most performance increase of CBC over IBC. Simulation conditions: 5 cm bucket, moderate turbulence, 60 kW array, LOS$_T$ = 0, σ_T = 0, σ_p = 0 or 0.4λ, BQ = 1.0, and no AO.

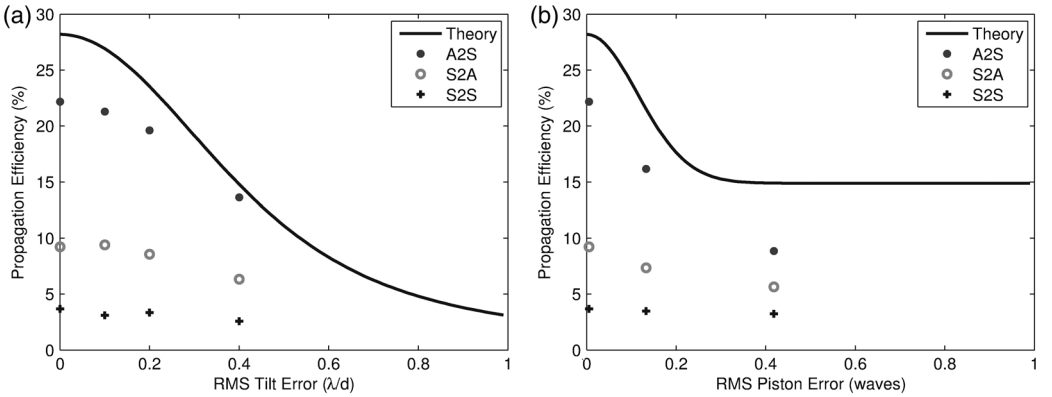

Fig. 14 Theory and simulation BPE results for 7.5 km slant range, moderate turbulence, and a 5 cm bucket versus (a) σ_T and (b) σ_p with $\mathrm{LOS}_T = 0$, $\mathrm{BQ} = 1$, and no AO. Note that the theory curve has been adjusted down for atmospheric extinction.

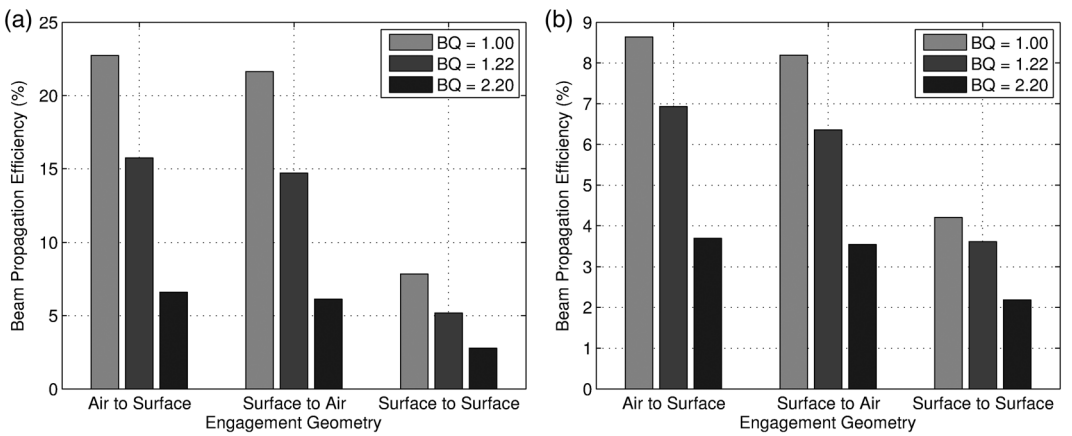

Fig. 15 BPE for a 5 cm bucket is significantly reduced due to changes in subaperture beam quality. Results for CBC are shown in (a) and those for IBC are in (b) (note the scale change between the two figures). Simulation conditions: 7.5 km range, 5 cm bucket, moderate turbulence, 60 kW array, $\mathrm{LOS}_T = 0$, $\sigma_T = 0$, $\sigma_p = 0$, and no AO.

defined as full aperture tilt jitter, LOS_T. Since a poorer BQ will cause a spreading of the far field beam, BQ is varied in conjunction with full aperture tilt to investigate the performance combination of these two effects.

Figure 16(a) shows the BPE with $\mathrm{LOS}_T = 5$ urad (RMS) for all three engagements and $\mathrm{BQ} = 1.0$, 1.22, and 2.20. These results are compared to zero LOS_T in Fig. 15 reprinted to the left of Fig. 16(a) for easy reference. It can be seen that LOS_T significantly reduces BPE from 22% to 12% for the A2S scenario with $\mathrm{BQ} = 1$. S2A and S2S result show similar drops in performance due to LOS_T and all scenarios show similar percentage drops in BPE with BQ reductions as seen without a full aperture tilt (Fig. 15). It should be noted that the jitter being $1.6\lambda/D$ is high and demonstrates that BQ cannot be relaxed without reducing performance even in the presence of large tilt RMS's.

The same comparison is made in Fig. 17 for the IBC case. For the IBC case the impact of LOS_T jitter is reduced since the diffraction angle is much larger, approximately three times that of the CBC. Both simulations were run under the same conditions of moderate turbulence.

Figure 18 completes the sensitivity for IBC. The turbulence is high, the full aperture pointing error is high with $\mathrm{LOS}_T = 1.66\lambda/D$, the subaperture pointing error is moderate with, $\sigma_T = 0.2\lambda/d$, and σ_p is near zero at 0.01λ. The high turbulence dominates the reduction in performance, but all effects contribute to a reduction in performance which is considered not viable (BPE <10%) for all scenarios except A2S. However, even under these conditions, a reduction in beam quality is still measureable for A2S and S2A. Note these results do not use AO, and BPE is now measured over a 10 cm bucket. The fact that AO is not employed and the larger, 10 cm bucket is used, favors a reduction in sensitivity to BQ changes, yet the results still show an impact on performance for these two scenarios. For the A2S engagement, reducing BQ from 1.0 to 2.2 reduces BPE by 52%. These results are presented for completeness, but it is questionable that a system with such a low BPE would be considered useful once it falls well below 10%. Therefore, for any tactical laser system, beam quality will be a major driver of overall system performance.

5.4 *Impact of Adaptive Optics*

Simulation results show the addition of an AO system significantly improves the performance of both CBC and IBC. The design used in the analysis has an actuator spacing of 2.0 cm in exit pupil space. Using a Fried geometry, this has approximately 5 actuators across each 10.0 cm diameter beamlet. Figure 19 presents AO performance for coherent combination for the moderate turbulence case as subaperture tilt [Fig. 19(a)] and piston jitter [Fig. 19(b)] are added. The

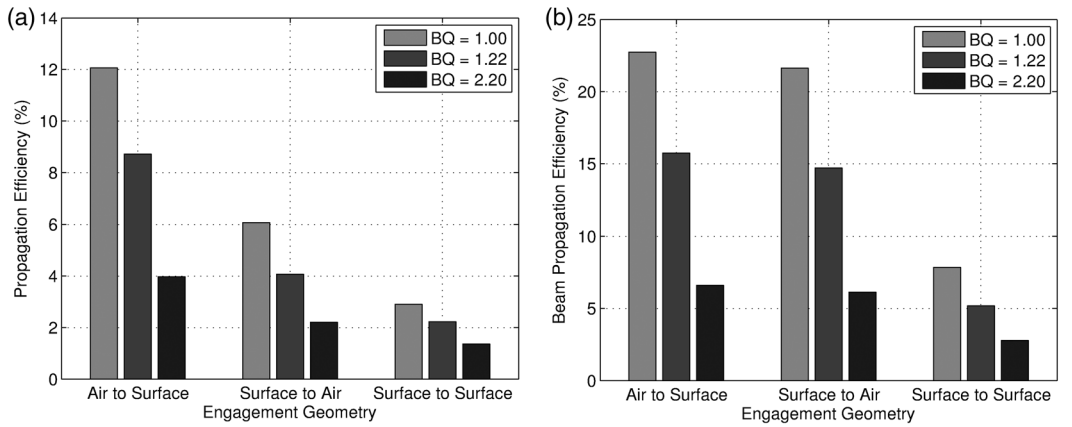

Fig. 16 BPE for CBC with (a) 5 urad RMS platform jitter, when compared with (b) no platform jitter, shows that platform jitter does significantly degrade performance of the coherent array. Simulation conditions: 7.5 km range, 5 cm bucket, moderate turbulence, 60 kW array, $\mathrm{LOS}_T = 1.66\lambda/D$ (left only), $\sigma_T = 0$, $\sigma_p = 0$, and no AO.

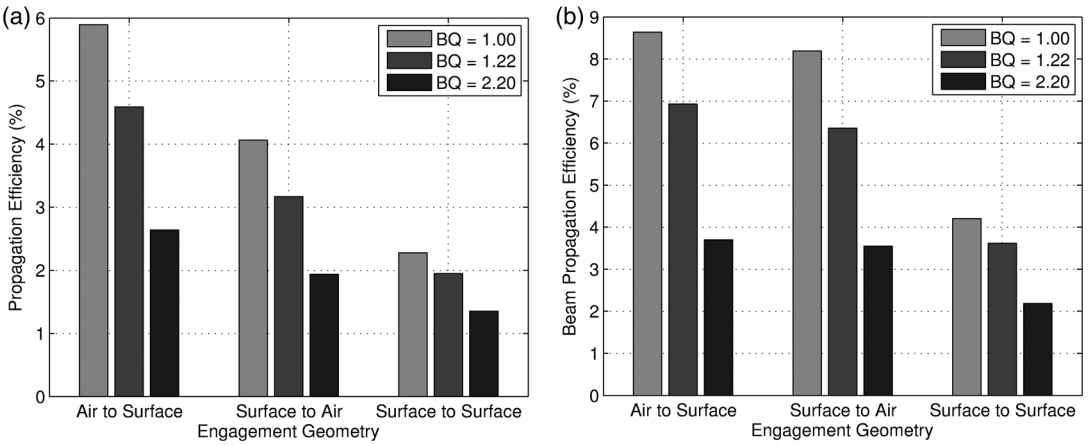

Fig. 17 BPE for IBC with (a) 5 urad RMS platform jitter, compared with (b) no platform jitter, shows that platform jitter degrades performance of IBC noticeably less than that of the coherent array. Simulation conditions: 7.5 km range, 5 cm bucket, moderate turbulence, 60 kW array, $\mathrm{LOS}_T = 1.66\lambda/D$ (left only), $\sigma_T = 0$, $\sigma_p = 0.4\lambda$, and no AO.

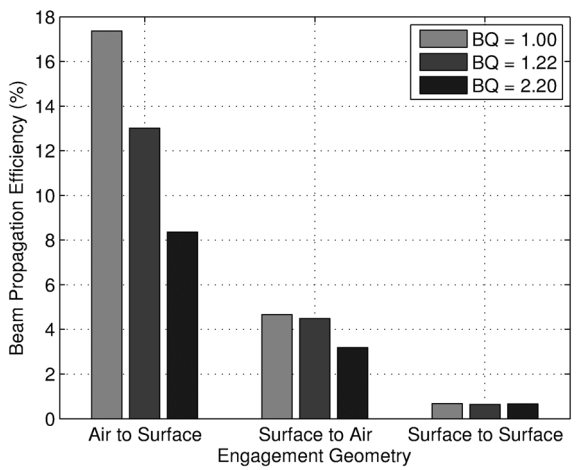

Fig. 18 BPE of IBC system under multiple effects and with a 10 cm bucket to show that BQ still has a measureable impact on performance. Performance decreases significantly due to poor beam quality for both A2S and S2A. Simulation conditions: 7.5 km range, 10 cm bucket, high turbulence, 60 kW array, $\mathrm{LOS}_T = 1.66\lambda/D$, $\sigma_T = 0.2\lambda/d$, $\sigma_p = 0.01\lambda$, and no AO.

A2S scenario has the highest BPE before AO is applied and, as expected, its performance changes the least with the addition of AO.

The addition of AO in the A2S scenario has little impact on performance improvement since the turbulence strength; in this case, being stronger closer to the target has little impact on irradiance in the target plane. Note, however, for the other scenarios that AO consistently improves the performance of CBC for both tilt and piston jitter. In these cases the performance increase is due to the correction of the higher order atmospheric effects and pupil mismatch.

With AO employed, the phasing loops are the only difference between CBC and IBC and, thus, the sensitivity plot of Fig. 19(b) can be used to compare CBC and IBC with AO. Referencing this figure, it can be seen that piston jitter at 0.4λ can be directly compared to CBC-performance points to the left of 0.28λ. Since the AO subsystem does not correct for residual subaperture piston jitter (thus, the downward trend in Fig. 19(b), this is the only difference between IBC and CBC. With this mind, the lower IBC performance can be understood in terms of adaptive optics where the individual beamlets are subapertures of a full aperture AO system, but in this case, subaperture tilt is only corrected. Hardy

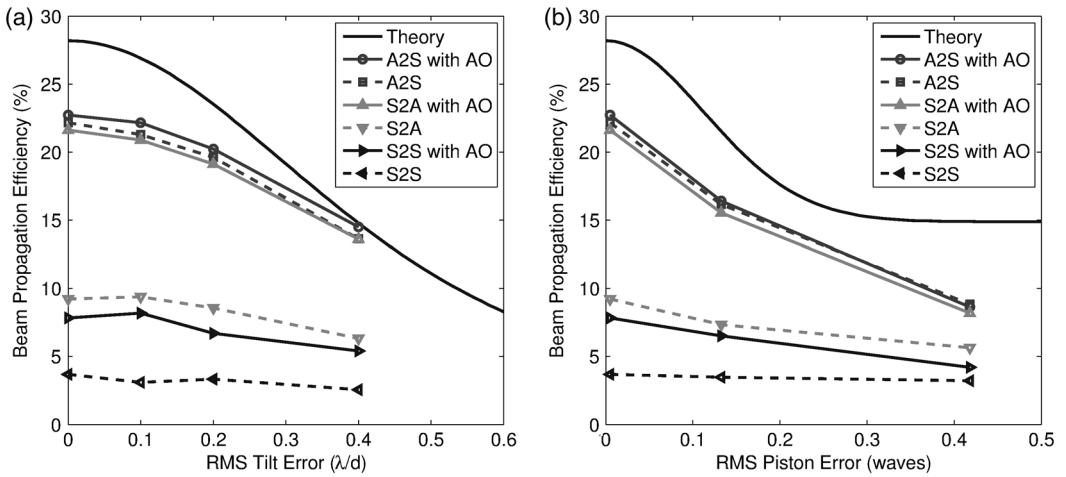

Fig. 19 BPE both with and without adaptive optics for varying (a) tilt and (b) piston errors, moderate turbulence, 200 Hz AO error rejection (see Table 5 for Greenwood frequency). Adaptive optics improves performance for both CBC and IBC for all scenarios. Simulation conditions: 7.5 km range, 5 cm bucket, moderate turbulence, 60 kW array, $\mathrm{LOS}_T = 0$, σ_T and σ_p as shown, and BQ = 1.0.

remarks that piston errors between subapertures in an AO subsystem are more detrimental than subaperture tilts in AO corrections.[27] The higher order phase across the full aperture of CBC and IBC, including tilt errors due to pupil mismatch, are corrected up to the random piston over each beamlet. Considering the individual beamlets of the IBC as a sparse AO subsystem the observation from Hardy provides another way to understand the performance difference between CBC and IBC when AO is used. Figure 20 summarizes the performance increase with the inclusion of AO. As explained, AO improves both S2A and S2S significantly in moderate turbulence with little impact on A2S.

Figure 21 presents the impact of AO on BPE for the high turbulence profile. The turbulence profiles were previously defined in Figs. 10 and 11. The results presented used the larger bucket at 10 cm to show that CBC still out performs IBC even for high turbulence and for a moderately sized target area. Recall that as the angular extent of the bucket increases, IBC performance will approach CBC. The S2S scenario for a range of 7.5 km and with high turbulence is out of reach with conventional AO. S2A shows significant improvement since the turbulence, weighted closer to the exit pupil of the transmitter, can be corrected more easily than the other scenarios. Conversely, the turbulence being weighted further from the transmitting aperture for the A2S shows little change in performance.

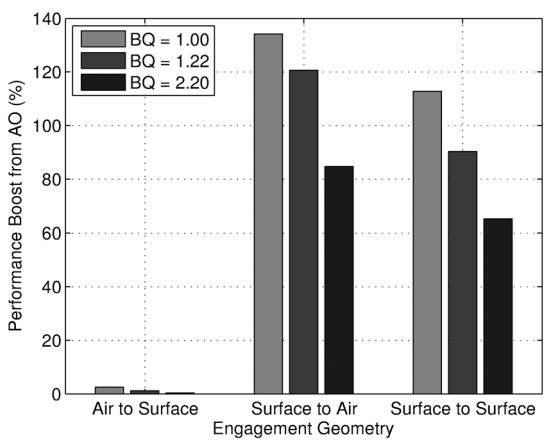

Fig. 20 The percentage increase in BPE with the inclusion of AO versus engagement and BQ for CBC and the moderate turbulence case. AO greatly improves performance for the S2A and S2S engagements. Simulation conditions: 7.5 km range, 5 cm bucket, moderate turbulence, 60 kW array, $\mathrm{LOS}_T = 0$, $\sigma_T = 0$, and $\sigma_p = 0$.

5.5 *Impact of Thermal Blooming*

Thermal blooming is the nonlinear interaction of the beam intensity with the atmosphere. The localized heating of the air, as the beam transits to the target, changes the index of refraction and causes a distortion of the beam along its path. The salient features of tilt and astigmatism in the far field spot can only be partially corrected for with an AO subsystem. The increased density of the lower atmosphere makes this effect more severe as the path becomes more horizontal. In this section the sensitivity to thermal blooming is investigated. All results presented previously included this effect inherent to the atmosphere. In the results

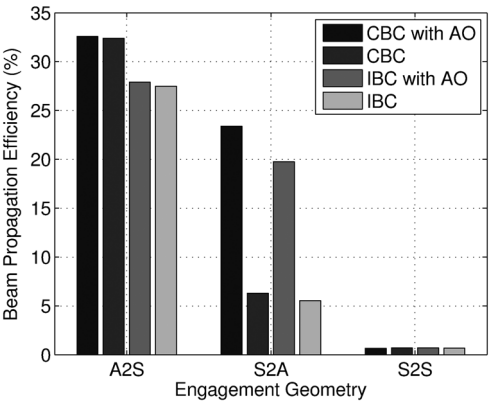

Fig. 21 BPE under high turbulence for CBC and IBC with and without adaptive optics (AO with a 200 Hz error rejection, see Table 5 for Greenwood frequencies). Adaptive optics improves performance for both CBC and IBC for scenarios with high turbulence except for the S2S scenario. The values shown for S2S are statistically zero for the confidence levels determined for this analysis. Simulation conditions: 7.5 km range, 10 cm bucket, high turbulence, 60 kW array, $\mathrm{LOS}_T = 0$, $\sigma_T = 0$, $\sigma_p = 0$ or 0.4λ, and BQ = 1.0.

to follow the comparison is made with thermal blooming turned off and on within the simulation.

The magnitude of thermal blooming has traditionally been qualitatively defined with the distortion number, N_d. Definitions of N_d vary in the literature depending on the author's preference as to which effects are most important to model. The definition chosen for this work is described in Ref. 5. The integral for N_d is defined in Eq. (5). This equation is based on a monolithic beam, thus, it is presented here with the cautionary note that its fidelity in representing a multilaser beam has not yet been evaluated. In addition to N_d, another parameter that gauges the effect of thermal blooming is critical power. This is the level of power above which the effect of thermal blooming dominates transmission and any further increase in power could cause even less power to arrive on target.[5]

$$N_d = 4\sqrt{2}Pk\frac{(n_0-1)}{C_p\rho_0}\int_0^{\text{Path}} dz \frac{\alpha_{\text{abs}}(z)\tau(z)}{T(z)D(z)v_\perp(z)}, \tag{5}$$

where P is power out of the aperture, k is $2\pi/\lambda$, n_0 is the refractive index of the undisturbed atmsophere, C_p is the specific heat at constant pressure, ρ_0 is the air density at mean sea level, α_{abs} is the absorbtion coefficient, $T(z)$ is the temperature of the air, $D(z)$ is the diameter of the beam along the path, $v_\perp(z)$ is the effective crosswind along the path, and $\tau(z)$ is the transmission along the path.

The distortion numbers and critical powers for the three scenarios and the two power levels used in this work are shown in Table 7. Figure 22(a) and 22(b) shows the performance decrease in BPE for CBC and IBC for a 60 and 150 kW array, respectively. The 60 kW power level shows minimal impact on BPE for all scenarios due to thermal blooming. The largest magnitude in reduction due to thermal blooming occurs for the A2S scenario at the 150 kW level with a reduction in BPE from 24% to 16%. This dramatic decrease in performance is most likely due to the following. The reduction of the turbulence strength with an increase in altitude favors the A2S scenario. But, unlike the turbulence, the absorption within the boundary layer is fairly constant in altitude, thus, the A2S beam, less spread than in the other two scenarios, will bloom more due to the beam's higher power density. The S2A and the S2S have been degraded already by the turbulence and, thus, show much lower reduction due to thermal blooming.

Table 7 N_d and critical power (kW) levels for the three scenarios at 7.5 km slant range.

Engagement	Air to surface		Surface to air		Surface to surface	
Power level (kW)	60	150	60	150	60	150
N_d	14	37	16	42	40	101
Critical power (kW)	111	105	97	93	39	38

The distortion numbers and critical powers calculated for these scenarios are not consistent with the simulation results. A full explanation is still being explored, but two comments are appropriate. First, the starting performance for all IBC scenarios are low (10% or lower) and adding the additional effect of thermal blooming has low impact. Second, it appears that use of the Eq. (5) over estimates the reduction in performance for a laser array.

5.6 *Analysis of System Performance*

This section selects nominal values for the set of parameters used in the previous sensitivity studies and reports the performance for the three scenarios as a function of range, both with and without AO included. This last look at performance is restricted to the CBC since it has been shown to be an upper bound for IBC for all previously presented results.

Figure 23 presents performance for the three scenarios as a function of range with all disturbances included and set to reasonable values listed in Table 8. A far field pattern provided to the right of Fig. 23 shows a BPE of ~10%. This is an average of far field performance for the A2S scenario at a range of 7.5 km. Given a 10% BPE as a minimally accepted performance, the maximum ranges for the three scenarios are presented in Table 9.

6 Summary

This paper provides a framework to study the performance tradeoffs for CBC and IBC. The design is not optimized for

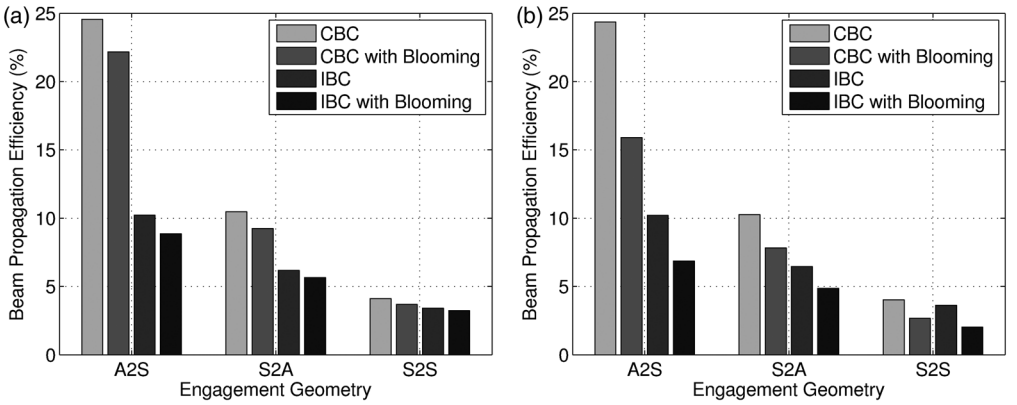

Fig. 22 BPE with and without the effects of thermal blooming on CBC and IBC. (a) The 60 kW system and (b) the 150 kW system. For the A2S CBC case, thermal blooming reduced BPE from 24 to 22 for the 60 kW array and from 24 to 16 for 150 kW array (all numbers percentages). Simulation conditions: are 7.5 km range, 5 cm bucket, moderate turbulence, $\text{LOS}_T = 0$, $\sigma_T = 0$, $\sigma_p = 0$ or 0.4λ, BQ = 1.0, and no AO.

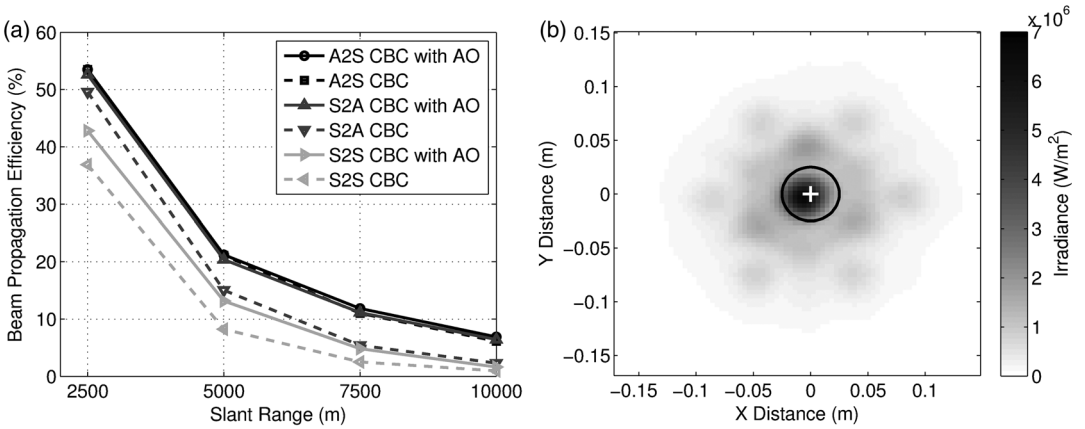

Fig. 23 CBC BPE performance for all disturbances set to nominal values listed in Table 8. The far-field spot in the upper right is for the A2S case with AO closed loop. The circle represents the 5 cm bucket that captures ~10% of the transmitted power for the 7.5 km slant range.

coherent beam combining, but rather was based on previous architectures in the literature. More importantly, this pupil geometry allows for a clear presentation of the tradeoffs between coherent and incoherent beam combining.

The adaption of previous work by Butts[18] provides an analytical description that captures both configurations, CBC and IBC, in a single equation. The tuning of a single parameter, σ_p, that models random phase between the individual beamlets, allows for a direct comparison in a vacuum of the two systems without approximation. Additionally, the analytical model provides a first-cut at setting design requirements for acceptable levels of subaperture RMS piston and tilt errors.

The same equation can be numerically integrated to calculate the performance metric of beam propagation efficiency, BPE. This metric captures the performance effect that best describes the transmitter performance in depositing energy within a defined bucket size in the far field. The analytical form is restricted to the vacuum case, but numerically integrated, it is used as an envelope of performance for follow-on wave optics simulation.

For identical pupil configurations, CBC typically performs better than IBC. The analysis shows this is true for bucket radii that are a few times the diffraction-limited width of the full aperture far-field spot. The effects of varying fill factor and aperture size when comparing CBC and IBC is explained within the report. A graphical presentation (Fig. 6) clearly demonstrates the tradeoff.

Three scenarios were evaluated to cover the complete set of generic tactical operations. Realistic power levels of the waveguide lasers for the beamlets were chosen for a 60 kW system and soon-to-be-demonstrated levels were considered for a 150 kW system. A median atmosphere for transmission was chosen from a worldwide database to maintain a consistent set of atmospheric parameters. A modified Hufnagel-Valley turbulence profile better accounting for the heating of the earth's boundary layer provided two atmospheres with moderate and high turbulence for a morning and afternoon scenario time, respectively.

The moderate turbulence atmosphere was used for the majority of the analysis. Performance was degraded significantly under the high turbulence atmosphere (Fig. 16), and the very low BPE numbers that resulted suggest that conventional AO is inadequate for this condition, except for S2A. The S2S scenario, not surprisingly the most stressing of the three, was dominated by turbulence degradation, even for moderate turbulence.

The impact of poor BQ was evaluated under moderate to severe conditions, including system random errors and high turbulence conditions. Beam quality significantly affected performance under all reasonable turbulence levels. In comparison, the impact from typical levels of platform jitter was found to be less significant (Fig. 17). In all cases evaluated, a poorer BQ decreased performance. This conclusion implies that BQ, as a system performance parameter, may not

Table 8 Nominal system parameters.

Parameter	Setting
Power	60 kW
Turbulence	Moderate
LOS_T	$0.3\lambda/D$
σT,	$0.1\lambda/d$
σp	0.1λ
BQ	1.22
AO	200 Hz
Tracker	320 Hz

Table 9 Maximum range for CBC with a BPE of at least 10%.

Scenario	Max range (>10% BPE, no AO)	Max range (>10% BPE, with AO)
Air to surface	~8 km	~8 km
Surface to air	~6 km	~8 km
Surface to surface	~4.5 km	~6 km

combine with other debilitating effects in a typical root-sum-square relationship.

Subaperture jitter, σ_T, was of minor significance if limited to 2 μrad RMS or less (Fig. 7). In the S2A scenario, this required the addition of an AO loop to reduce tilt errors due to pupil mismatch. For the A2S scenario, the inclusion of AO had little impact on performance because the turbulence was weighted closer to the target (Fig. 7).

For the sake of brevity and clarity, the analysis in this report did not vary fill factor. The main point concerning fill factor is embodied in Fig. 6 where the effects of its change and changing aperture size are graphically displayed. This figure clearly shows the significant degrader that fill factor can be on a phased array system. The design used within this study could be improved significantly for the coherent beam combining case with improvements in fill factor. However, the analysis presented on BPE can be adjusted easily for arbitrary fill factors by increasing these numbers by the ratio of the new fill factor to the one used in this report.

Acknowledgments

This work was funded by a grant from the High Energy Laser Joint Technology Office (HEL JTO) and the Air Force Office of Scientific Research (AFOSR). The authors acknowledge the contribution of Dr. Matthew Whiteley, MZA Dayton Office, for constructing the WaveTrain model and his expert advice in running the simulations. This research was supported in part by an appointment to the Postgraduate Research Participation Program at the Air Force Institute of Technology administered by the Oak Ridge Institute for Science and Education through an interagency agreement between the U.S. Department of Energy and AFIT. The views expressed in this paper are those of the authors and do not necessarily reflect the official policy or position of the Air Force, the Department of Defense, or the U. S. Government.

References

1. J. A. Tirpak, "Laser horizons," *Air Force Mag.* **95**(4), 37–39 (2012).
2. R. A. Motes and R. W. Berdine, *Introduction to High-Power Fiber Lasers*, Directed Energy Professional Society, Albuquerque, New Mexico (2009).
3. S. J. Augst et al., "Beam combining of ytterbium fiber amplifiers," *J. Opt. Soc. Am.* **24**(8), 1707–1712 (2007).
4. P. Sprangle et al., "Incoherent combining and atmospheric propagation of high-power fiber lasers for directed-energy applications," *IEEE J. Quantum Electron.* **45**(2), 138–139 (2009).
5. G. P. Perram et al., *Introduction to Laser Weapon Systems*, Directed Energy Professional Society, Albuquerque, New Mexico (2010).
6. T. Y. Fan, "Laser beam combining for high-power, high radiance sources," *IEEE J. Sel. Top. Quantum Electron.* **11**(3), 567–575 (2005).
7. P. Zhou et al., "Numerical analysis of the effects of aberrations on coherently combined fiber laser beams," *Appl. Opt.* **47**(18), 3350–3356 (2008).
8. B. N. Pulford, "LOCSET phase locking: operation, diagnostics, and applications," PhD Thesis, Optical Science & Engineering, University of New Mexico, Albuquerque (2012); R. R. Butts, "Effects of piston and tilt errors on the performance of multiple mirror telescopes," *Proc. SPIE* **293**, 85–89 (1981).
9. T. M. Shay, "Theoretical model for self-synchronous locking of optical coherence by single-detector electronic-frequency tagging," *Conf. Lasers Electro-Optics, OSA* (2007).
10. D. Mordaunt, D. Filgas, and M. Cox, Raytheon Company, El Segundo, CA, private communication (2012).
11. D. Figas et al., "Recent results for the Raytheon RELI program," *Proc. SPIE* **8381**, 83810W (2012).
12. J. C. Marron, "Spatially processed image detection and ranging (SPIDAR)," *IEEE Lasers and Electro-Optics Society, LEOS 21st Annual Meeeting*, pp. 509–510 (2008).
13. D. P. Greenwood, "Tracking turbulence-induced tilt errors with shared and adjacent apertures," *J. Opt. Soc. Am.* **67**(3), 282–289 (1977).
14. D. P. Greenwood and D. L. Fried, "Power spectra requirements for wave-front-compensative systems," *J. Opt. Soc. Am.* **66**(3), 193–206 (1976).
15. S. Basu and D. Voelz, "Tracking in a ground to satellite optical link: effects due to lead ahead and aperture mismatch, including temporal tracking response," *J. Opt. Soc. Am. A* **25**(7), 1594–1608 (2008).
16. P. F. McManamon et al., "A review of phased array steering for narrow-band electrooptical systems," *Proc. IEEE* **97**(6), 1078–1096 (2009).
17. P. Sprangle et al., "Incoherent combining of high-power fiber lasers for long-range directed-energy applications," *J. Directed Energy* **2**(3), 273–284 (2007).
18. R. R. Butts, "Effects of piston and tilt errors on the performance of multiple mirror telescopes," *Proc. SPIE* **293**, 85–89 (1981).
19. P. Zhou et al., "Optimal truncation of element beam in a coherent fiber laser array," *Chin. Phys. Lett.* **26**(4), 044206-1–044206-3 (2009).
20. J. B. Shellan, "Phased-array performance degradation due to mirror misfigures, piston errors, jitter, and polarization errors," *J. Opt. Soc. Am.* **2**(4), 555–556 (1985).
21. C. D. Nabors, "Effects of phase errors on coherent emitter arrays," *Appl. Opt.* **33**(12), 2284–2289 (1994).
22. J. W. Goodman, *Introduction to Fourier Optics*, 3rd ed., Roberts & Company, Greenwood Village, Colorado (2005).
23. A. E. Siegman, *Lasers*, University Science Books, Sausalito, California (1986).
24. H. T. Yura, "Optimum truncation of a Gaussian beam in the presence of random jitter," *J. Opt. Soc. Am.* **12**(2), 375–378 (1995).
25. S. T. Fiorino et al., "Broad-spectrum optical turbulence assessments from climatological temperature, pressure, humidity, and wind," *J. Directed Energy* **3**(3), 223–238 (2010).
26. S. T. Fiorino et al., "Validation of a worldwide physics-based, high spectral resolution atmospheric characterization and propagation package for UV to RF wavelengths," *Proc. SPIE* **7090**, 709001 (2008).
27. J. W. Hardy, *Adaptive Optics for Astronomical Telescopes*, Oxford University Press, New York, NY(1998), "Test results: Ytterbium laser system, YLS-10000-SM, S/N 10052950," IPG-Oxford (Oct. 2011).

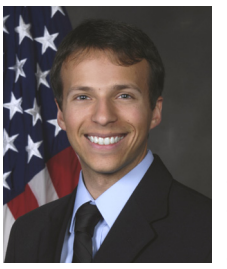

Noah R. Van Zandt received his BS degree in electrical engineering from Cedarville University with highest honors in 2010. Currently, he is a research assistant with the Center for Directed Energy within the Engineering Physics Department at the Air Force Institute of Technology (AFIT) in Dayton, Ohio. His research interests include atmospheric propagation of HELs, tracking of airborne targets, beam combination methods, and solid state lasers.

Salvatore J. Cusumano received his PhD in control theory from the University of Illinois in 1988, an MSEE from the Air Force Institute of Technology in 1977, and a BSEE from the United States Air Force Academy in 1971. He currently serves as assistant professor of Optics and Beam Control within the Engineering Physics Department at the Air Force Institute of Technology. He is also an active member of the Center for Directed Energy. His research interests are manifested in his 30 years of experience in directed energy and include resonator alignment and stabilization, intra-cavity adaptive optics, phased arrays, telescope control, pointing and tracking, adaptive optics, and component technology for directed energy. He holds two patents (jointly) for his work in phased arrays.

Richard J. Bartell received his BS degree in physics from the U.S. Air Force Academy as a distinguished graduate in 1979. He received his MS degree from the Optical Sciences Center, University of Arizona, in 1987. He was a research physicist with the Center for Directed Energy of the Air Force Institute of Technology when this work was performed. He is currently a spectral scientist and senior technical expert for Riverside Research.

Santasri Basu received her PhD in electrical engineering with a specialization in optics in 2008 and her MSEE in 2005, both from New Mexico State University. She received her BSEE with honors from Jadavpur University, India in 2000. Currently she is a research associate at the Air Force Institute of Technology's Center for Directed Energy within the Engineering Physics Department. Her research interests include adaptive optics, telescope pointing and tracking, rough surface scattering, and laser communications. Prior to working at AFIT, she was a visiting assistant professor in the Department of Physics and Optical Engineering at Rose-Hulman Institute of Technology.

Jack E. McCrae, Jr received his PhD in physics from the Air Force Institute of Technology in 1997, an MS in physics (optics) from the Air Force Institute of Technology in 1993, and a BS in physics from the Massachusetts Institute of Technology in 1984. He is a retired Air Force Colonel with 27 years of service and currently a senior research associate with the Center for Directed Energy within the Engineering Physics Department at AFIT. His research interests include optics, lasers, quantum and non-linear optics, laser radar, atmospheric propagation, and imaging.

Steven T. Fiorino received his BS degrees in geography and meteorology from Ohio State (1987) and Florida State (1989) universities. He additionally holds an MS in atmospheric dynamics from Ohio State (1993) and a PhD in physical meteorology from Florida State (2002). He is a retired Air Force Lieutenant Colonel with 21 years of service and currently a research associate professor of atmospheric physics within the Engineering Physics Department at AFIT and is the director of the Center for Directed Energy. His research interests include microwave remote sensing, development of weather signal processing algorithms, and atmospheric effects on military systems such as high-energy lasers and weapons of mass destruction.